Freesurfer-Initialized Large Deformation Diffeomorphic Metric Mapping with application to Parkinson's Disease

Jingyun Chen[a] Samantha J. Palmer[b] Ali R. Khan[a] Martin J. McKeown[b] Mirza Faisal Beg[a]

[a]School of Engineering Science, Simon Fraser University, 8888 University Drive, Burnaby BC, V5A 1S6, Canada;

[b]Pacific Parkinson's Research Centre, Brain Research Centre, University of British Columbia, Vancouver BC, V6T 2B5, Canada

ABSTRACT

We apply a recently developed automated brain segmentation method, FS+LDDMM, to brain MRI scans from Parkinson's Disease (PD) subjects, and normal age-matched controls and compare the results to manual segmentation done by trained neuroscientists. The data set consisted of 14 PD subjects and 12 age-matched control subjects without neurologic disease and comparison was done on six subcortical brain structures (left and right caudate, putamen and thalamus). Comparison between automatic and manual segmentation was based on Dice Similarity Coefficient (Overlap Percentage), L1 Error, Symmetrized Hausdorff Distance and Symmetrized Mean Surface Distance. Results suggest that FS+LDDMM is well-suited for subcortical structure segmentation and further shape analysis in Parkinson's Disease. The asymmetry of the Dice Similarity Coefficient over shape change is also discussed based on the observation and measurement of FS+LDDMM segmentation results.

Keywords: Computational Anatomy, Automated Segmentation, Parkinson's Disease, Freesurfer

1. INTRODUCTION

Parkinson's Disease is a neurodegenerative disorder that affects approximately 1% of the population above the age of 65. It causes movement symptoms such as tremor (shaking), rigidity (stiffness), slowness of movement and difficulty with balance. These symptoms are the result of disrupted transmission through dopaminergic pathways in the Basal ganglia. Therefore, it would be desirable in PD research to segment and analyze the Basal ganglia structures from clinical magnetic resonance brain scans.

The purpose of brain image segmentation is to assign a set of labels to different brain tissues or anatomical structures derived from brain images. Recently-developed brain image segmentation methods can be categorized into three general types. The first type is knowledge-based. This type of methods perform label assignment based on implicit or explicit anatomical knowledge, such as training sets and anatomical constraints (Pitiot et al.[1]), shape and positional information (Xia et al.[2]) and landmarks (Chupin et al.[3]). The second type is template-based. This type of methods segment target images by registering them to a pre-labeled template brain image, and perform the same transformation to the labels of the template. Shen et al. presented Hierarchical Attribute Matching Mechanism for elastic registration (HAMMER),[4] and used it in deformable registration of brain images. Klein et al. presented an automated method called Mindboggle based on a set of manually labeled brains registered to the subject brain as atlas.[5] The third type is probabilistic-based. This type of methods estimate label assignments that maximize a posteriori probability of classification under certain constraints. Gouttard et al. presented a segment method via a deformable registration of an unbiased atlas with probabilistic spatial priors.[6] Fischl et al. presented a set of brain MR image reconstruction tools called FreeSurfer(FS),[7] which transforms target brain scans into Talairach space and performs both cortical percolation and subcortical segmentation. Khan et al.[8] combined the probabilistic-based FS method with Large Deformation Diffeomorphic Metric Mapping (LDDMM) based label propagation,[9] and developed FS+LDDMM method. In this paper, we demonstrate how the FS+LDDMM method can be further used in subcortical structure segmentation for PD research.

Correspondent Author: Jingyun Chen (jingyunc@sfu.ca)

Medical Imaging 2009: Image Processing, edited by Josien P. W. Pluim, Benoit M. Dawant,
Proc. of SPIE Vol. 7259, 725931 · © 2009 SPIE
CCC code: 1605-7422/09/$18 · doi: 10.1117/12.810854

The paper is organized as follows. In Section 2 a full description of FS+LDDMM method and experimenting materials is given, followed by validation study design. In Section 3 the validation results are shown and discussed. In Section 4 conclusion is given and future work is introduced.

2. MATERIALS AND METHODS

2.1 Materials

We validate the FS+LDDMM method on 26 brain MRI data sets obtained from the Pacific Parkinson's Disease Research Center at the University of British Columbia. The data sets include scans of healthy control brains and PD brains. The PD data set consisted of 14 subjects (8 male, 6 female, 11 right-handed, mean age=66 years, SD=7.5). The mean symptom duration was 68.5 months, and the mean score on the motor portion of the Unified Parkinsons Disease Rating Scale (UPDRS) was 26.5, SD=9. The control subjects were 13 age-matched subjects with no neurological or psychiatric conditions (3 male, 10 female, 12 right-handed, mean age=58 years, SD=12).

High resolution structural (T1) images were acquired on a 3 Tesla scanner (Philips Achieva 3.0T; Philips Medical Systems, Netherlands) equipped with a head-coil (3DT1TFE CLEAR, TR=7.691ms, TE=3.58ms, flip angle=8, FOV=$256 \times 170 \times 200$mm). We acquired 170 slices axially parallel to the AC-PC plane.

Regions of interest (ROI) were outlined manually by an experienced neuroscience technologist using Amira software (Amira 3D Visualization and Volume Modeling V.3.1.1.). Boundaries were selected as defined in the Talairach atlas.[10]

The resolution of these brain images varies due to upgrades in the scanner made over the period of data collection. There are three types of images: $253 \times 253 \times 168$ with voxel size $1.0133 \times 1.0133 \times 1.0133$, $240 \times 240 \times 159$ with voxel size $1.06667 \times 1.06667 \times 1.06918$, and $240 \times 240 \times 144$ with voxel size $1 \times 1 \times 1$.

2.2 Image Segmentation Method

FS+LDDMM method is a segmentation-by-registration method. The method contains the following steps.

First, FreeSurfer establishes initial labels of the target structures, which mainly contains five stages: affine registration with Talairach space, initial volumetric labeling, bias field correction, non-linear alignment to the Talairach space, and final labeling of the volume.

Second, based on the FS labels, ROI containing all target structures, linearly aligned, are cropped from the original images, to reduce the computational intensity and avoid trapping in local minima during LDDMM.

At last, LDDMM computes the deformation from the ROI of template image to ROI of each target image, then uses that deformation to map the manual labels, on template image, to automatic labels (i.e. segmentations) on target images. The LDDMM optimization uses a three-stage-procedure, starting with Cerebrospinal Fluid (CSF) labels (i.e. the portion of the ventricles in ROI), followed by Gaussian smoothed ROI, and finally the original ROI. Each step initializes with the optimal map computed at the previous stage, to avoid potential local minima.

In summary, the FS+LDDMM method computes the deformation between FS initiated ROI of template and target images, then use the same deformation to propagate automatic labels from manual labels, as shown in Figure 1. For the details of LDDMM optimization and label propagation, please refer to Khan's paper.[8]

2.3 Validation Study Design

We use several comparison metrics to quantify the segmentation accuracy, as shown in Equation 1 - 6 and described in this section. The $L1$ error is defined in Equation 1, where we denote a manual segmentation by M and an automatic segmentation by A. The Dice Similarity Coefficient (DSC) is defined in Equation 2. where $V(A)$ is the volume of the segmented image A. It is assumed A and B are binary segmentations. For perfect spatial correspondence between the two binary images, $DSC = 1$, for no spatial correspondence, $DSC = 0$. We also computed the Symmetrized Hausdorff Distance and the Symmetrized Mean Surface Distance. The Directed Hausdorff Distance is defined in Equation 3, where $d(a, b)$ is the distance between points on two

different surfaces. To symmetrize this metric, we use Equation 4. The Hausdorff Distance gives an upper bound on the mismatch between the contours of segmentations. Directed mean surface distance is defined in Equation 5, and is symmetrized similarly as shown in Equation 6.

$$Error_{L1} = \frac{\|A - M\|_{L1}}{\|M\|_{L1}} = \frac{\sum_{x\in\Omega} \|A(x) - M(x)\|}{\sum_{x\in\Omega} \|M(x)\|} \tag{1}$$

$$DSC(A, B) = \frac{2V(A \cap B)}{V(A) + V(B)} \tag{2}$$

$$h(A, B) = \max_{a\in A} \min_{b\in B} d(a, b) \tag{3}$$

$$H(A, B) = \max\{h(A, B), h(B, A)\} \tag{4}$$

$$sd(A, B) = \frac{1}{N_A} \sum_{a\in A} \min_{b\in B} d(a, b) \tag{5}$$

$$SD(A, B) = max\{sd(A, B), sd(B, A)\} \tag{6}$$

3. RESULTS AND DISCUSSION

FS+LDDMM was performed on the brain data sets described in section 2.1 to segment six ROI including the caudate, thalamus, and putamen (both left and right). The computation was conducted on a SGI Altix 3700 server(64 Itanium CPU's, 64-bit, 64 GB RAM). FreeSurfer subcortical segmentations were computed with version 3.0.5 using 1-processor, with processing time for each subject in the range of 8 to 16 hours. LDDMM was performed using flows discretized to 20 timesteps, parallelized on 8-processors for each ROI. LDDMM run-times for each ROI were 72.6 ± 36.6 minutes (mean $\pm$ standard deviation) with a range of 24 to 180 minutes.

3.1 Overall Segmentation Quality

One typical set of segmentation are compared in Figure 2. Table 1 shows the overlap percentages (DSC and L1 error) of for FS+LDDMM and FS segmentations to manual segmentations, which is regarded as the "gold truth". Significant decreases in L1 error can be found in FS+LDDMM segmentations over FS for all ROI, which indicates FS+LDDMM segmentations have more similarity to manual segmentations than FS segmentations. Similarly, increase of DSC can be found in FS+LDDMM segmentations over FS for most ROI. Table 2 contains surface distances (the Hausdorff distance and mean surface distance) for FS+LDDMM and FS segmentations to manual segmentations. FS+LDDMM segmentations have smaller surface distances to manual segmentations over FS for all ROI , which again implies better segmentation accuracy of the FS+LDDMM method.

3.2 Varying Bias of DSC Metric

In the validation study we did not observe as much DSC improvement for FS+LDDMM segmentation as other similarity measurements. In Table 1 the change of DSC is slightly positive for most ROI and negative for some ROI such as right thalamus. One major cause of this issue is the dependence of DSC on subject sizes. A numerical simulation conducted by Rohlfing et al.[11] shows that DSC (defined as similarity index in the paper) depends strongly on subject sizes and is smaller for smaller subjects. Table 3 shows that in general, FS segmentations have larger volumes than manual segmentations, while FS+LDDMM segmentations have smaller volumes. In another word, FS method tends to "over-segments" a given ROI compared to the FS+LDDMM method, as shown in Figure 3. According to Rohlfing's argument, FS+LDDMM segmentations are more heavily penalized by DSC because they tend to have smaller volumes compared to FS-only.

To explore this potential bias of the DSC metric, we conducted a numerical simulation. We take the left caudate of the template and perform morphological operation on it. The structuring element is defined as a

$3 \times 3 \times 3$ cube, and dilation and erosion are performed once and twice to generate four different simulated volumes. Let the volume of the original structure $V(M) = 1$, and the increase or decrease generated by dilation or erosion be denoted as e. Then the dilated volume is $1 + e$. According to Equation 2, between original and dilated volume, $DSC = \frac{2\times1}{1+1+e} = \frac{2}{2+e}$. Similarly, erode volume becomes $1 - e$, and $DSC = \frac{2\times(1-e)}{1+1-e} = \frac{2-2e}{2-e}$. The change of DSC along e is plotted in Figure 4. From the plot we can see that for the same e the DSC is smaller for the eroded subjects, which agrees with Rohlfing's simulation. The bias of DSC grows as e grows. For the first time of morphological operation, e is approximately same for eroded and dilated subjects. However, dilated subject has a higher DSC. For the second time of operation, even though e is larger in dilated subjects, DSC is still larger than eroded subjects.

The same simulation is performed on left putamen and thalamus and the DSC's are computed for stimulated volumes to the template volumes. The results are shown in Figure 4. In summary, because of the general smaller volumes of ROI segmented by FS+LDDMM and larger volumes by FS, FS+LDDMM segmentations take more penalty by DSC metric, even if the FS+LDDMM method produces results that are more similar to manual segmentation as implied by other metrics.

4. CONCLUSION

This paper validates the recently developed FS+LDDMM method for subcortical MR image segmentation. FS+LDDMM method is used to segment six Basal ganglia structures that are relevant to Parkinson's disease. Qualitatively, there is a monotonic improvement in the surface smoothness of segmented ROI when comparing manual, FS-only. Qualitative evaluation of overlap percentages and surface distances to manual segmentations is also conducted on FS+LDDMM and FS methods. Under most measurements, FS+LDDMM shows general improvement over FS method alone on segmenting the majority of subjects. There is one metric (DSC) that does not indicate as significant improvement as other metrics. After theoretical analysis and simulative experiments we prove that this is mainly caused by the varying bias of the metric itself.

The future work for implementing FS+LDDMM in Parkinson's Disease research includes producing a more representative template brain. As FS+LDDMM is a template-based segmentation method, the segmenting accuracy depends strongly on the template selection strategy. Furthermore, FS+LDDMM computes initial momentum of deformation velocity field from each subject's ROI to the template, which can be considered as representation of the shape of that ROI. Analysis on these initial momenta may lead to automatic classification derived from the segmented ROI.

ACKNOWLEDGMENTS

This project is supported by the grant CHRP 75115. The authors would also like to thank Behrang Nosrat Makouei for his help in implementing Freesurfer, and Yan Lu for inspiration to creating this paper.

REFERENCES

[1] Pitiota, A., Delingettea, H., Thompson, P. M., and Ayachea, N., "Expert knowledge-guided segmentation system for brain mri," *NeuroImage* **23 Supplement 1**, S85–S96 (2004).

[2] Xia, Y., Bettinger, K., Shen, L., and Reiss, A., "Automatic segmentation of the caudate nucleus from human brain mr images," *Medical Imaging, IEEE Transactions on* **26**, 509–517 (April 2007).

[3] Chupin, M., Mukuna-Bantumbakulu, A. R., Hasboun, D., Bardinet, E., Baillet, S., Kinkingn'ehun, S., Lemieux, L., Dubois, B., and Garnerob, L., "Anatomically constrained region deformation for the automated segmentation of the hippocampus and the amygdala: Method and validation on controls and patients with alzheimer's disease," *Neuroimage* **34**, 995–1019 (2007).

[4] Shen, D. and Davatzikos, C., "Hammer: hierarchical attribute matching mechanism for elastic registration," *Medical Imaging, IEEE Transactions on* **21**(11), 1421–1439 (2002).

[5] Klein, A. and Hirsch, J., "Mindboggle: a scatterbrained approach to automate brain labeling," *NeuroImage* **24**, 261–280 (2005).

[6] Gouttard, S., Styner, M., Joshi, S., G.Smith, R., Hazlett, H. C., and Gerig, G., "Subcortical structure segmentation using probabilistic atlas priors," in [*SPIE*], (2007).

[7] Fischl, B., Salat, D. H., Busa, E., Albert, M., Dieterich, M., Haselgrove, C., van der Kouwe, A., Killiany, R., Kennedy, D., Klaveness, S., Montillo, A., Makris, N., Rosen, B., and Dale, A. M., "Whole brain segmentation: automated labeling of neuroanatomical structures in the human brain," *Neuron* **33**, 341–355 (2002).

[8] Khan, A. R., Wang, L., and Beg, M. F., "Freesurfer-initiated fully-automated subcortical brain segmentation in mri using large deformation diffeomorphic metric mapping," *NeuroImage* **41(3)**, 735–46 (2008).

[9] Beg, M. F., Miller, M. I., Trouv, A., and Younes, L., "Computing large deformation metric mappings via geodesic flows of diffeomorphisms," *International Journal of Computer Vision* **61**, 139–157 (2005).

[10] Talairach, J. and Tournoux, P., [*Co-Planar Stereotaxic Atlas of the Human Brain: 3-Dimensional Proportional System - an Approach to Cerebral Imaging*], Thieme Medical Publishers (1988).

[11] Rohlfing, T., Brandtb, R., Menzelb, R., and Calvin R. Maurer, J., "Evaluation of atlas selection strategies for atlas-based image segmentation with application to confocal microscopy images of bee brains," *NeuroImage* **21**, 1428–1442 (2004 April).

APPENDIX A. FIGURES AND TABLES

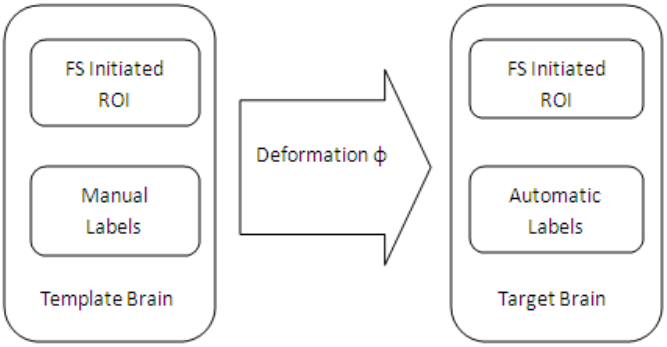

Figure 1. Illustration of FS+LDDMM method. Note that the inverse deformation is used to find out which coordinates from template brain each voxel of segmentation result comes from. Usually the coordinates point to non-grid locations in template brains and interpolation is require. Using the deformation directly can not guarantee each voxel in template brain be mapped to a grid location in target brain.

Table 1. Average DSC's and L1 errors of FS segmentations and LDDMM segmentations, using manual segmentations as references.

Structure/Manual volume	Method	Volume	DSC	L1 error
Left Caudate/	FS	3818 ± 556.12	0.68 ± 0.08	0.38 ± 0.16
3177 ± 999.36	FS+LDDMM	2899 ± 443.94	0.75 ± 0.07	0.24 ± 0.07
Left Putamen/	FS	5246 ± 751.23	0.65 ± 0.11	0.51 ± 0.26
3330 ± 1254.47	FS+LDDMM	2077 ± 517.83	0.67 ± 0.11	0.27 ± 0.06
Left Thalamus/	FS	7186 ± 838.22	0.73 ± 0.08	0.37 ± 0.21
4840 ± 1131.67	FS+LDDMM	4410 ± 514.89	0.74 ± 0.06	0.26 ± 0.10
Right Caudate/	FS	3586 ± 523.71	0.68 ± 0.06	0.34 ± 0.12
3282 ± 978.63	FS+LDDMM	3176 ± 432.14	0.71 ± 0.06	0.29 ± 0.08
Right Putamen/	FS	4803 ± 786.12	0.69 ± 0.09	0.40 ± 0.21
3439 ± 1278.78	FS+LDDMM	3388 ± 648.38	0.71 ± 0.06	0.30 ± 0.09
Right Thalamus/	FS	6942 ± 668.06	0.74 ± 0.07	0.33 ± 0.18
5175 ± 1193.04	FS+LDDMM	5005 ± 523.20	0.72 ± 0.08	0.29 ± 0.12

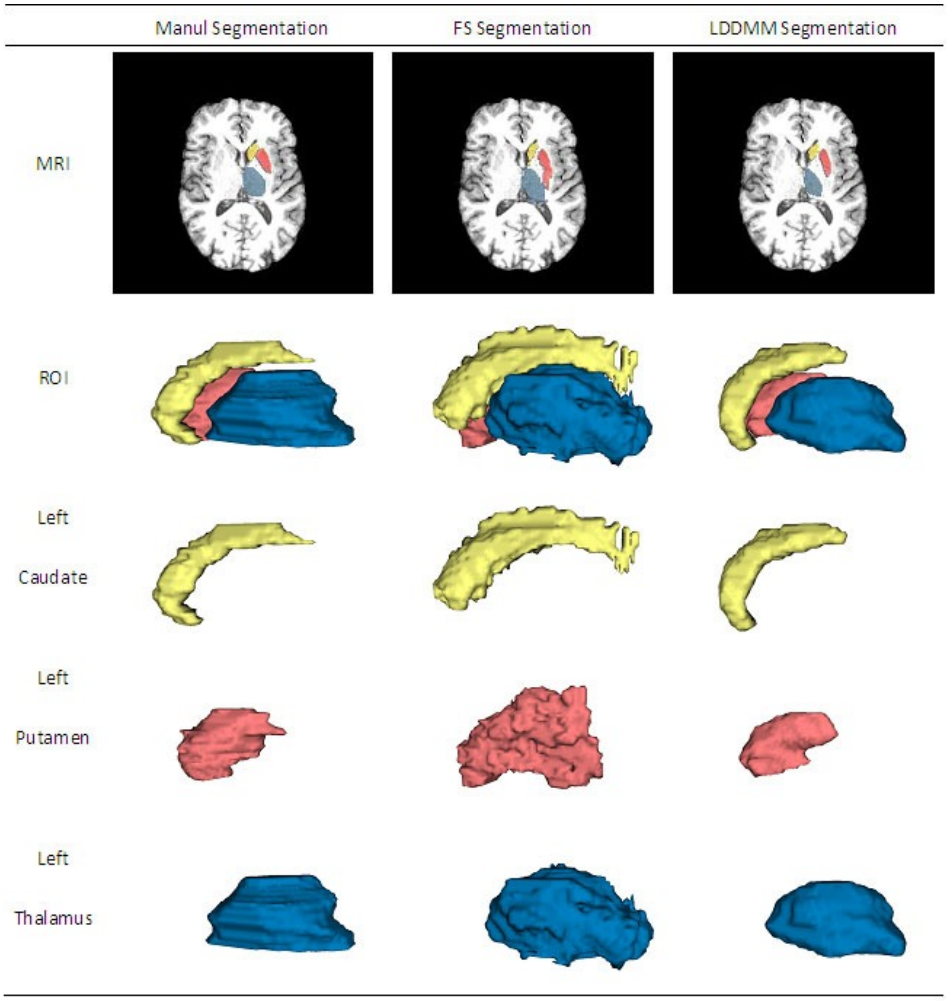

Figure 2. Comparison of segmentations. From the left column to the right contain manual segmentations, FS segmentations and FS+LDDMM segmentations correspondingly. The first row from upside contains the original brain MRI slices overlapped by segmenting results (Transverse view). From the second to fifth row contain 3D volumes for the three ROI on left side (Sagittal view). The second row is three ROI posed in respective positions. The third row is caudate, fourth row is putamen and fifth row is thalamus.

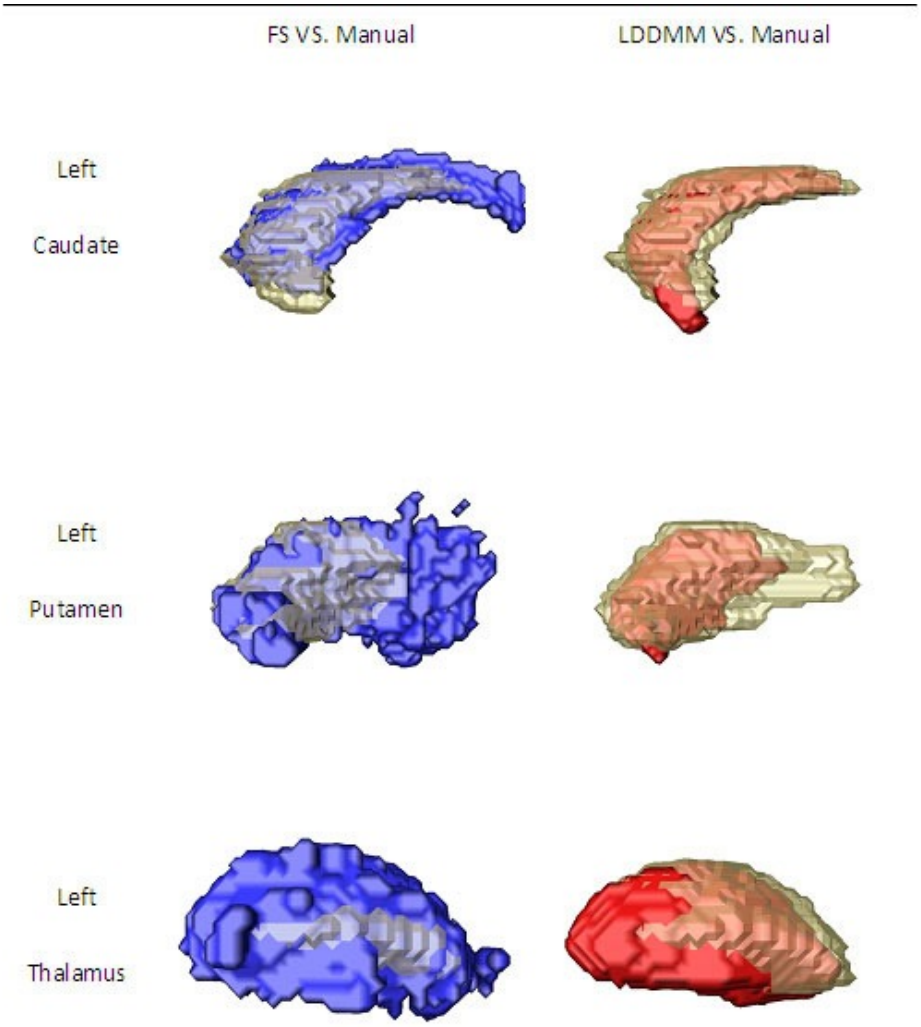

Figure 3. Illustration of FS's over-segmentation and LDDMM's under-segmentation. The left column is FS segmentations (blue) overlapping on manual segmentations (transparent). The right column is FS+LDDMM segmentations (red) overlapping on manual segmentations (transparent). The first row from upside is caudate, the second is putamen, the third is thalamus

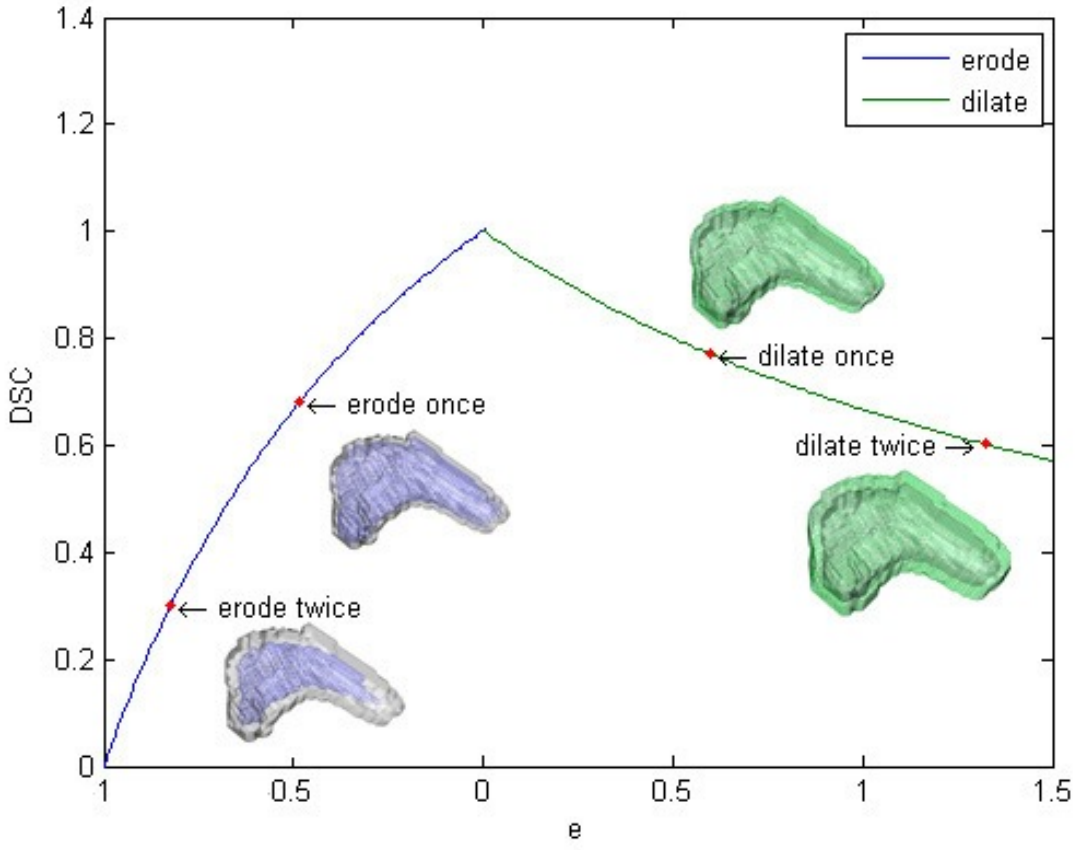

Figure 4. DSC changes over subject erosion and dilation. The left curve (blue) represents the DSC change over erosion, where $DSC = \frac{2-2e}{2-e}$, e denotes the volume difference from the original structure. The right curve (green) represents the DSC change over dilation, where $DSC = \frac{2}{2+e}$.

Table 2. Average Hausdorff distances and mean surface distances of FS segmentations and FS+LDDMM segmentations, using manual segmentations as references.

Structure	Method	sym hausdorff	sym 95% hausdorff	sym mean surf dist
Left Caudate	FS	16.85 ± 5.86	12.01 ± 5.94	2.92 ± 1.59
	FS+LDDMM	6.68 ± 3.27	4.41 ± 2.64	1.38 ± 0.63
Left Putamen	FS	11.93 ± 3.49	8.76 ± 3.26	2.90 ± 1.29
	FS+LDDMM	8.36 ± 3.93	5.85 ± 3.17	1.95 ± 0.97
Left Thalamus	FS	7.44 ± 1.59	5.27 ± 1.51	2.11 ± 0.67
	FS+LDDMM	5.86 ± 1.54	4.35 ± 1.21	1.65 ± 0.40
Right Caudate	FS	16.26 ± 5.41	10.63 ± 4.98	2.57 ± 1.21
	FS+LDDMM	6.98 ± 3.71	4.44 ± 2.65	1.52 ± 0.66
Right Putamen	FS	10.84 ± 3.72	8.16 ± 3.52	2.46 ± 1.18
	FS+LDDMM	7.56 ± 2.64	5.23 ± 2.02	1.76 ± 0.55
Right Thalamus	FS	7.33 ± 2.17	4.93 ± 1.82	1.98 ± 0.67
	FS+LDDMM	6.71 ± 1.56	4.72 ± 1.46	1.88 ± 0.53

Table 3. Average volumes and DSC's of the three left ROI.

Structure	Manual volume	FS volume	LDDMM volume	FS DSC	LDDMM DSC
Left Caudate	3177 ± 999.36	3818 ± 556.12	2899 ± 443.94	0.68 ± 0.07	0.75 ± 0.07
Left Putamen	3330 ± 1254.47	5246 ± 751.23	2077 ± 517.83	0.65 ± 0.11	0.67 ± 0.11
Left Thalamus	4840 ± 1131.67	7186 ± 838.22	4410 ± 514.89	0.73 ± 0.08	0.74 ± 0.06

Table 4. DSC's of the morphologically operated ROI to the original ROI.

	erode once	dilate once	erode twice	dilate twice
Left Caudate	0.6800	0.7703	0.3020	0.6018
Left Putamen	0.6680	0.7633	0.2829	0.5927
Left Thalamus	0.7767	0.8175	0.5239	0.6702